PROCEEDINGS OF SCIENCE

Recent heavy ion results from the ATLAS experiment

Rikard SANDSTRÖM*, **on behalf of the ATLAS Collaboration**
Max Planck Institut für Physik, Munich
E-mail: rikard.sandstrom@cern.ch

During the first three years of operation the ATLAS experiment has collected an integrated luminosity of 0.15 nb^{-1} for $\sqrt{s_{NN}} = 2.76$ TeV lead-lead collisions, 30 nb^{-1} for 5.02 TeV proton-lead collisions, and 5 pb^{-1} for $\sqrt{s} = 2.76$ TeV proton-proton collisions. The proton-lead and the high-statistics 2.76 TeV proton-proton data recorded during the highly successful 2013 LHC heavy ion run provide valuable control measurements for interpreting results from lead-lead collisions. Measurements of bulk particle production are presented with the focus on studies of elliptic and higher-order collective flow coefficients. Included in these results are measurements of event-by-event collective flow. In addition to providing baseline measurements for the lead-lead program, the proton-lead data also provide a unique opportunity to study the physics of soft and hard processes in a high parton density environment. Two-particle correlations in relative azimuthal angle $(\Delta\phi)$ and pseudorapidity $(\Delta\eta)$ measured in $\sqrt{s_{NN}} = 5.02$ TeV p+Pb collisions are presented.

The European Physical Society Conference on High Energy Physics -EPS-HEP2013
18-24 July 2013
Stockholm, Sweden

*Speaker.

PoS(EPS-HEP 2013)193

1. Flow harmonics in Pb+Pb collisions

Heavy ion collisions at the Relativistic Heavy Ion Collider (RHIC) and the Large Hadron Collider (LHC) create hot, dense matter that is thought to be composed of strongly interacting quarks and gluons. A useful tool to study the properties of this matter is the azimuthal anisotropy of particle emission in the transverse plane. This anisotropy is believed to result from pressure-driven anisotropic expansion (referred to as "flow") of the created matter, and is described by a Fourier expansion of the particle distribution in azimuthal angle ϕ, around the beam direction

$$\frac{\mathrm{d}N}{\mathrm{d}\phi} \propto 1 + 2\sum_{i=1}^{\infty} v_n \cos n(\phi - \Phi_n) \tag{1.1}$$

where v_n and Φ_n represent the magnitude and phase of the n^{th}-order anisotropy. These quantities can also be conveniently represented by the per-particle "flow vector": $\overrightarrow{v_n} = (v_n \cos n\Phi_n, v_n \sin n\Phi_n)$.

In typical non-central heavy ion collisions, the large and dominating v_2 coefficient is associated mainly with the "elliptic" shape of the nuclear overlap. However, v_2 in central (head-on) collisions and the other v_n coefficients in general are related to various shape components of the initial state arising from fluctuations of the nucleon positions in the overlap region. The large pressure gradients and ensuing hydrodynamic evolution can convert these shape components into v_n coefficients in momentum space. Calculations based on viscous hydrodynamics suggest that v_n scales nearly linearly with shape eccentricity ε_n , for n < 4.

Most previous measurements estimate v_n from the distribution of particles relative to the event plane, accumulated over many events. This event-averaged v_n mainly reflects the hydrodynamic response of the created matter to the average collision geometry in the initial state. More information, however, can be obtained by measuring $\overrightarrow{v_n}$ or v_n on an event-by-event basis.

The distributions of v_2, v_3 and v_4 have been measured with the ATLAS detector [1] over a broad range of centrality in lead–lead (Pb+Pb) collisions at $\sqrt{s_{NN}} = 2.76$ TeV [2]. The observed v_n distributions are measured using charged particles in the pseudorapidity range $|\eta| < 2.5$ and the transverse momentum range $p_{\mathrm{T}} > 0.5$ GeV, which are then unfolded to estimate the true v_n distributions.

To illustrate the level of event-by-event fluctuations in the data, the top panels of Figure 1 show the azimuthal distribution of charged particle tracks with $p_{\mathrm{T}} > 0.5$ GeV for three typical events in the 0–5% centrality interval. The corresponding track-pair $\Delta\phi$ distributions from the same events are shown in the bottom panels. For each pair of particles two $\Delta\phi$ entries, $|\phi_1 - \phi_2|$ and $-|\phi_1 - \phi_2|$, are made each with a weight of 1/2, and then folded into the $[-0.5\pi, 1.5\pi]$ interval. Patterns beyond the structures in the event-averaged distributions, shown by the solid points, are observed. These event-by-event distributions are the inputs to the event-by-event v_n analyses.

The azimuthal distribution of particles in Figure 1 needs to be corrected for non-uniform detector acceptance. An acceptance function is obtained from the ϕ distribution of all tracks in all events, which is Fourier expanded. The observed v_n is from a first order Taylor expansion

$$v_{n,i}^{\mathrm{obs}} = v_{n,i}^{\mathrm{raw}} - v_{n,i}^{\mathrm{det}}, \quad i = x, y \tag{1.2}$$

where the values of detector effects $v_{n,i}^{\mathrm{det}}$ are less than 0.007 for $2 \leq n \leq 4$. Higher order corrections were found to give negligible contribution to final v_n for $2 \leq n \leq 4$.

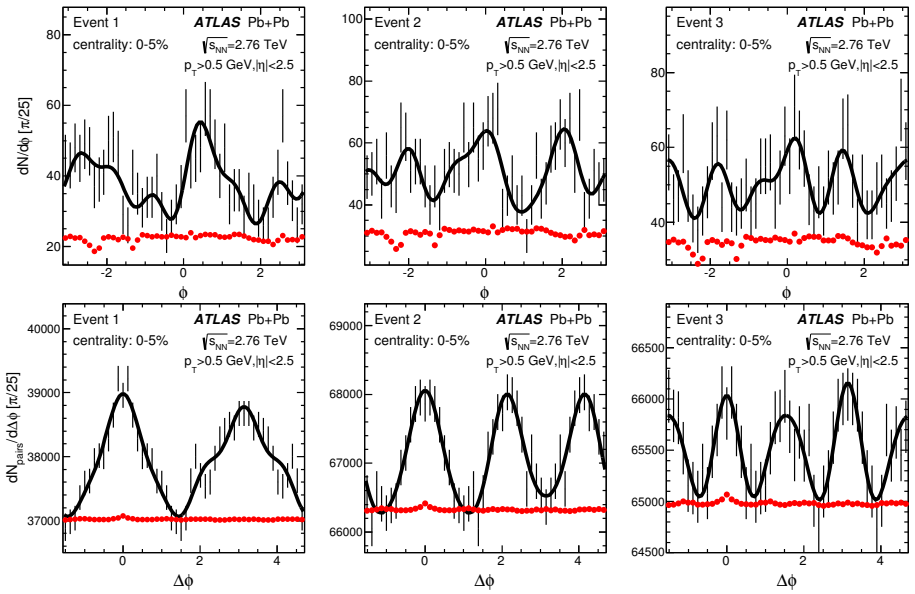

Figure 1: Single-track ϕ (top) and track-pair $\Delta\phi$ (bottom) distributions for three typical events (from left to right) in the 0–5% centrality interval. The bars indicate the statistical uncertainties of the foreground distributions, the solid curves indicate a Fourier parameterization including the first six harmonics: $dN/d\phi = A(1+2\sum_{i=1}^{6} c_n \cos n(\phi - \Phi_n))$ for single-track distributions and $dN/d\Delta\phi = A(1+2\sum_{i=1}^{6} c_n \cos n(\Delta\phi))$ for track-pair distributions, and the solid points indicate the event-averaged distributions (arbitrary normalization).

Due to the finite track multiplicity, the measured flow vector is expected to be smeared randomly around the true flow vector by a 2D response function $p(\vec{v}_n^{\,\mathrm{obs}}|\vec{v}_n)$. By dividing an event into two hemispheres with respect to $\eta = O$, the distribution of the difference of flow coefficients between the two hemispheres is obtained. The physical flow signal cancels in this distribution such that it contains mainly the effects of statistical smearing and non-flow. Denoting the width of the x and y projections of the distribution of flow vector difference between the two hemispheres by δ_{2SE}, the width δ of the response function is $\delta_{2SE}/\sqrt{2}$ for the full detector, or $\delta_{2SE}/2$ for a hemisphere, while the response function is

$$p(\vec{v}_n^{\,\mathrm{obs}}|\vec{v}_n) \propto e^{-\frac{(\vec{v}_n^{\,\mathrm{obs}} - \vec{v}_n)^2}{2\delta^2}}. \tag{1.3}$$

Figure 2 compares the event-by-event v_2 distributions with the distributions of the eccentricity ε_2 of the initial geometry, calculated from the Glauber model [3] and the MC-KLN model [4]. The MC-KLN model is based on the Glauber model but takes into account the corrections to the initial geometry due to gluon saturation effects. The ε_2 distribution for each centrality interval is rescaled to match the v_2 of the data, and then normalized to form a probability density function. Since v_2 is expected to be proportional to ε_2 in most hydrodynamic calculations, the deviation between the v_2 distributions and the rescaled ε_2 distributions can be used to improve the modeling of the initial geometry. Figure 2 shows that the rescaled ε_2 distributions describe the data well for the most central collisions, but not so well for non-central collisions. In peripheral collisions, both the Glauber and MC-KLN models fail to describe the data. A smaller scale factor is generally

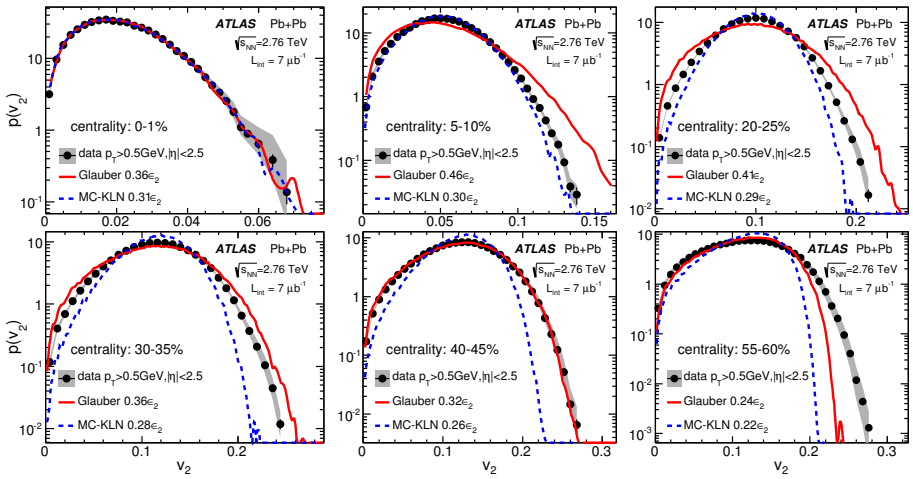

Figure 2: The *event-by-event* v_2 distributions compared with the ε_2 distributions from two initial geometry models: a Glauber model (solid lines) and the MC-KLN model (dashed lines). The ε_2 distributions have been rescaled to the same mean values. The scale factors are indicated in the legends.

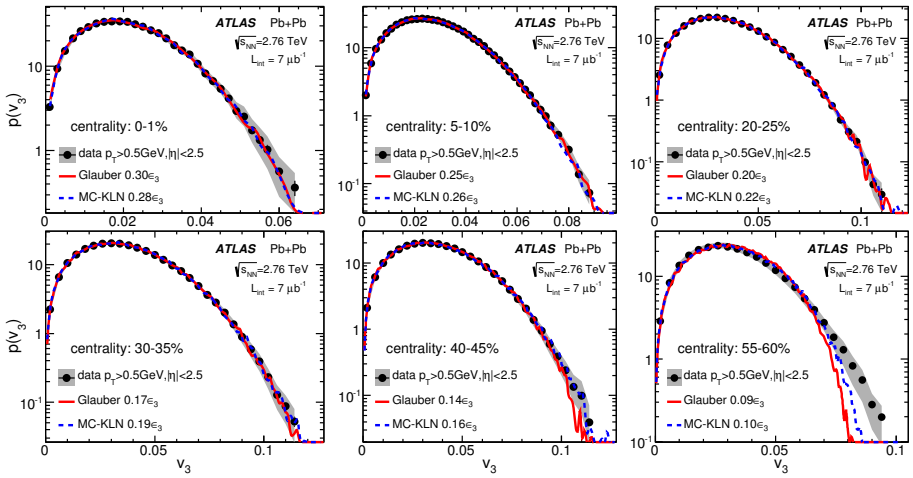

Figure 3: The *event-by-event* v_3 distributions compared with the ε_3 distributions from two initial geometry models: a Glauber model (solid lines) and the MC-KLN model (dashed lines). The ε_3 distributions have been rescaled to the same mean values. The scale factors are indicated in the legends.

required for the MC-KLN model, reflecting the fact that the ε_2 values from the MC-KLN model are on average larger than those from the Glauber model. Similar comparisons between v_3 and ε_3 are shown in Figure 3. Agreement with the models is better than in the $n = 2$ case. However, this could simply reflect the fact that these distributions are dominated by Gaussian fluctuations, which have a universal shape.

2. Two-particle angular correlations

An important tool to probe the physics of these events is the two-particle correlation function measured in terms of the relative pseudorapidity $(\Delta\eta)$ and azimuthal angle $(\Delta\phi)$ of selected particle

pairs, $C(\Delta\eta,\Delta\phi)$. The first studies of two-particle correlation functions in the highest-multiplicity $p+p$ collisions at the LHC showed an enhanced production of pairs of particles at $\Delta\phi \sim 0$, with the correlation extending over a wide range in $\Delta\eta$, a feature frequently referred to as a "ridge" [5]. Many of the physics mechanisms proposed to explain the $p+p$ ridge, including multi-parton interactions, parton saturation, and collective expansion of the final state, are also expected to be relevant in p+Pb collisions.

The two-particle angular correlation has been studied with the ATLAS experiment over $|\Delta\eta| < 5$ in p+Pb collisions, based on an integrated luminosity of approximately 1 μb^{-1} recorded during a short run in September 2012 [6]. The LHC was configured with a 4 TeV proton beam and a 1.57 TeV per-nucleon Pb beam that together produced collisions with a nucleon–nucleon center-of-mass energy of $\sqrt{s_{NN}} = 5.02$ TeV and a rapidity shift of -0.47 relative to the ATLAS rest frame.

The correlation functions are given by

$$C(\Delta\phi,\Delta\eta) = \frac{S(\Delta\phi,\Delta\eta)}{B(\Delta\phi,\Delta\eta)}, \quad C(\Delta\phi) = \frac{S(\Delta\phi)}{B(\Delta\phi)}, \tag{2.1}$$

where S represents pair distributions constructed from the same event, B from "mixed events", and $\Delta\phi = \phi_a - \phi_b$ and $\Delta\eta = \eta_a - \eta_b$ are the angular differences between particle a and particle b. The mixed-event distribution, $B(\Delta\phi,\Delta\eta)$, that measures uncorrelated pair yields was constructed by choosing pairs of particles from different events of similar impact parameter and track multiplicity, to match the effects of detector acceptance, occupancy, and material on $S(\Delta\phi,\Delta\eta)$, and of similar $\sum E_{\text{T}}^{\text{Pb}}$, the sum of transverse energy in the forward calorimeter in the direction of the Pb beam.

Examples of 2D correlation functions are shown in Figures 4(a) and (b) for charged particles with $0.5 < p_{\text{T}}^{a,b} < 4$ GeV in peripheral and central events. The correlation function for peripheral events shows a sharp peak centered at $(\Delta\phi,\Delta\eta) = (0,0)$ due to pairs originating from the same jet, Bose-Einstein correlations, as well as high-p_{T} resonance decays, and a broad structure at $\Delta\phi \sim \pi$ from dijets, low-p_{T} resonances, and momentum conservation. In central events, the correlation function reveals a ridge-like structure at $\Delta\phi \sim 0$ range (the "near-side"). The distribution at $\Delta\phi \sim \pi$ (the "away-side") that extends over the full measured $\Delta\eta$ is also broadened relative to peripheral events, consistent with the presence of a long-range component in addition to that seen in peripheral events.

The strength of the long-range component is quantified by the "per-trigger yield", $Y(\Delta\phi)$, which measures the average number of particles correlated with each trigger particle, folded into the $0-\pi$ range [6]. Figure 4(c) shows the $Y(\Delta\phi)$ distributions for $2 < |\Delta\eta| < 5$ in peripheral and central events separately. The yield for peripheral events has an approximate $1-\cos\Delta\phi$ shape with an away-side maximum, characteristic of a recoil contribution. In contrast, the yield in central events has near-side and away-side peaks with the away-side peak having a larger magnitude. These features are consistent with the onset of a significant $\cos 2\Delta\phi$ component in the distribution. To quantify further the properties of these long-range components, the distributions are integrated over $|\Delta\phi| < \pi/3$ and $|\Delta\phi| > 2\pi/3$, and plotted as a function of $\sum E_{\text{T}}^{\text{Pb}}$ in Figure 4(d) The near-side yield is close to 0 for $\sum E_{\text{T}}^{\text{Pb}} < 20$ GeV and increases with $\sum E_{\text{T}}^{\text{Pb}}$. The away-side yield shows a similar variation as a function of $\sum E_{\text{T}}^{\text{Pb}}$, except that it starts at a value significantly above zero, even for events with low $\sum E_{\text{T}}^{\text{Pb}}$. The yield difference between these two regions is found to be

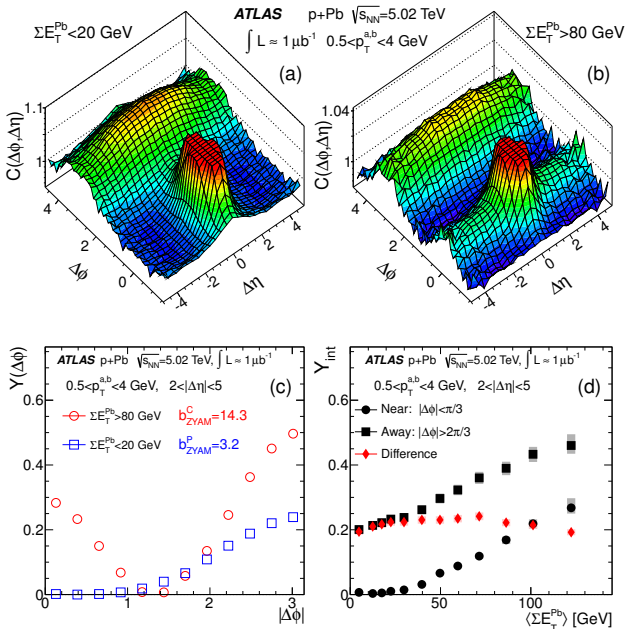

Figure 4: Two-dimensional correlation functions for (a) peripheral events and (b) central events, both with a truncated maximum to suppress the large correlation at $(\Delta\eta,\Delta\phi) = (0,0)$; (c) the per-trigger yield $\Delta\phi$ distribution together with pedestal levels for peripheral ($b^{\mathrm{P}}_{\mathrm{ZYAM}}$) and central ($b^{\mathrm{C}}_{\mathrm{ZYAM}}$) events, and (d) integrated per-trigger yield as function of $\sum E_{\mathrm{T}}^{\mathrm{Pb}}$ for pairs in $2 < |\Delta\eta| < 5$. The shaded boxes represent the systematic uncertainties, and the statistical uncertainties are smaller than the symbols.

approximately independent of $\sum E_{\mathrm{T}}^{\mathrm{Pb}}$, indicating that the growth in the yield with increasing $\sum E_{\mathrm{T}}^{\mathrm{Pb}}$ is the same on the near-side and away-side.

The $Y(\Delta\phi)$ distributions for peripheral and central events, as well as their difference, $\Delta Y(\Delta\phi)$, are shown in Figure 5 in various p^a_{T} ranges with $0.5 < p^b_{\mathrm{T}} < 4$ GeV. This difference is observed to be nearly symmetric around $\Delta\phi = \pi/2$. To illustrate this symmetry, the $\Delta Y(\Delta\phi)$ distributions in Figure 5 are overlaid with functions $a_0 + 2a_2\cos 2\Delta\phi$ and $a_0 + 2a_2\cos 2\Delta\phi + 2a_3\cos 3\Delta\phi$, with the coefficients calculated as $a_n = \Delta Y(\Delta\phi)\cos n\Delta\phi$. Using only the a_0 and a_2 terms describes the ΔY distributions reasonably well, indicating that the long-range component of the two-particle correlations can be approximately described by a recoil contribution plus a $\Delta\phi$-symmetric component. The inclusion of the a_3 term improves slightly the agreement with the data.

3. Summary and conclusions

Measurements of the event-by-event harmonic flow coefficients v_n for $n = 2$, 3 and 4 for various centrality intervals have been performed using 7 $\mu\mathrm{b}^{-1}$ of Pb+Pb collision data at $\sqrt{s_{NN}} = 2.76$ TeV collected by the ATLAS experiment at the LHC. The v_2 distributions approach that of a radial projection of a 2D Gaussian distribution centred around zero in the 0-2% centrality range, which is consistent with a scenario where fluctuations are the primary contribution to the overall shape (fluctuation-only scenario) for these most central collisions. Starting with the centrality interval 5-10%, the v_2 distributions differ significantly from this scenario, suggesting that they have a significant component associated with the average collision geometry in the reaction plane.

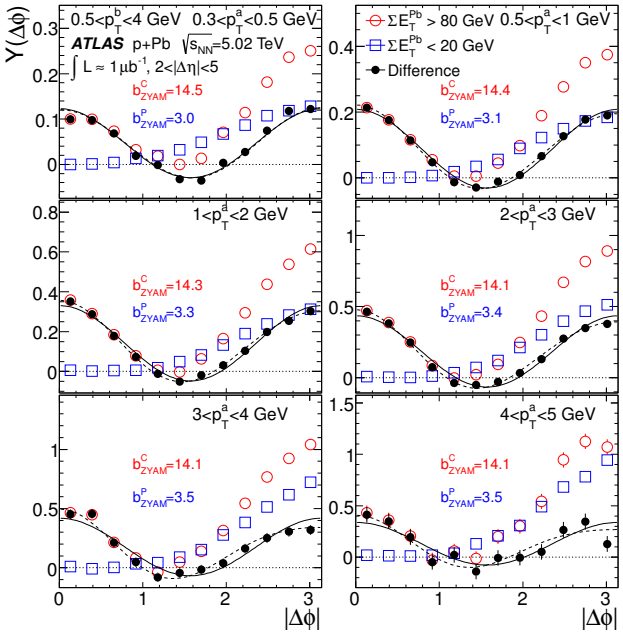

Figure 5: Distributions of per-trigger yield in the peripheral and the central event activity classes and their differences (solid symbols), for different ranges of p_{T}^{a} and $0.5 < p_{\mathrm{T}}^{b} < 4$ GeV, together with functions $a_0 + 2a_2 \cos 2\Delta\phi$ (solid line) and $a_0 + 2a_2 \cos 2\Delta\phi + 2a_3 \cos 3\Delta\phi$ (dashed line) obtained via a Fourier decomposition. The values for the ZYAM-determined pedestal levels are indicated on each panel for peripheral ($b^{\mathrm{P}}_{\mathrm{ZYAM}}$) and central ($b^{\mathrm{C}}_{\mathrm{ZYAM}}$) $\sum E_{\mathrm{T}}^{\mathrm{Pb}}$ bins.

In contrast, the v_3 and v_4 distributions are consistent with a pure 2D Gaussian-fluctuation scenario over most of the measured centrality range.

Using 1 $\mu\mathrm{b}^{-1}$ p+Pb at $\sqrt{s_{NN}} = 5.02$ TeV an away-side contribution was observed with the ATLAS detector that grows rapidly with increasing $\sum E_{\mathrm{T}}^{\mathrm{Pb}}$ and which matches many essential features of the near-side ridge observed here, as well as in previous high-multiplicity $p+p$, p+Pb and Pb+Pb data at the LHC. Thus, while the ridge in $p+p$ and p+Pb collisions has been characterized as a near-side phenomenon, these results show that it has both near-side and away-side components that are symmetric around $\Delta\phi \sim \pi/2$, with a $\Delta\phi$ dependence that is approximately described by a $\cos 2\Delta\phi$ modulation. A Fourier decomposition of the correlation function, $C(\Delta\phi)$, yields a pair $\cos 2\Delta\phi$ amplitude of about 0.01 at $p_{\mathrm{T}} \sim 3$ GeV, corresponding to a single-particle amplitude of about 0.1.

References

[1] ATLAS Collaboration, JINST **3** (2008) S08003.

[2] ATLAS Collaboration, JHEP **1311** (2013) 183 arXiv:1305.2942 [hep-ex].

[3] M. L. Miller *et al.* Ann. Rev. Nucl. Part. Sci. 57 (2007) 205, arXiv:0701025 [nucl-ex].

[4] H.-J. Drescher *et al.* Phys. Rev. C74 (2006) 044905, arXiv:0605012 [nucl-th].

[5] CMS Collaboration, JHEP **1009** (2010) 091 arXiv:1009.4122 [hep-ex].

[6] ATLAS Collaboration, Phys. Rev. Lett. **110** (2013) 182302 arXiv:1212.5198 [hep-ex].